ORIGINAL PAPER

Effect of SiO_2 and B_2O_3 on crystallization and structure of CaF_2–CaO–Al_2O_3-based slag for electroslag remelting of ultra-supercritical rotor steel

Yi Huang[1] · Cheng-bin Shi[1] · Xiu-xiu Wan[1] · Jiang-ling Li[2] · Ding-li Zheng[3] · Jing Li[1]

Abstract

Regarding development of the dedicated slag for electroslag remelting, crystallization characteristics of the slag exert a strong influence on the initial solidification of liquid metal in mold and surface quality of as-cast ingot. The crystallization behavior of CaF_2–CaO–Al_2O_3-based slag with varying SiO_2 and B_2O_3 contents and their correlation with the slag structure were investigated. Increasing SiO_2 (0.24–8.95 mass%) and B_2O_3 (0–3.20 mass%) contents lowers the crystallization temperature and suppresses the crystallization of the slag melts, as well as decreases the sizes of the crystalline phases. The crystalline phases precipitated during continuous cooling of the slag melts are faceted $11CaO \cdot 7Al_2O_3 \cdot CaF_2$, faceted or spherical CaF_2, and non-faceted $MgO \cdot Al_2O_3$ (or MgO) in sequence irrespective of the SiO_2 and B_2O_3 contents of the slag. The polymerization degree of slag melts increases with increasing either SiO_2 or B_2O_3 contents. The crystallization of the slag melts is increasingly retarded with increasing the SiO_2 and B_2O_3 contents of the slag caused by increased component diffusion resistance originating from increased polymerization degree of the slag melts.

Keywords Crystallization · Slag structure · Polymerization degree · Electroslag remelting · Ultra-supercritical rotor steel

1 Introduction

Rotor is the core component of steam turbine in power plants. Great efforts have been made to developing steam turbine rotor steels and their manufacturing technologies for ultra-supercritical (USC) power plants in order to increase the thermal efficiency of coal-fired power generation and reduce CO_2 emissions [1–3]. The typical steel grades are FB2 and MarBN steels used up to 630 and

650 °C. Electroslag remelting (ESR) is an indispensable process in the production of ultra-supercritical rotor steels. According to the steel nominal compositions, minimizing the aluminum pickup (< 0.010 mass% in the ingot) and preventing boron loss during ESR of ultra-supercritical rotor steels are mandatory requirements [4, 5]. However, boron loss and aluminum pickup during liquid steel refining have always been one of the extremely serious issues in the production of rotor steel for ultra-supercritical steam turbines [6–8]. The change in the concentrations of these alloying elements is closely related to the slag compositions, originating from slag-steel reactions [6–8].

ESR-type slags are CaF_2–CaO–Al_2O_3-based system generally containing 40−70 mass% CaF_2, 20−30 mass% Al_2O_3, 20−30 mass% CaO, 2 mass% MgO and minor amounts of tramp oxides SiO_2 and FeO (SiO_2 + FeO < 2 mass%). For ESR of some steels, TiO_2, Ce_2O_3 and/or SiO_2 are intentionally added to tailor the slag for the specific requirements [9–12]. The functions of the slag in ESR process have been summarized elsewhere [12]. For ESR of rotor steels, it is suggested that a certain amount of B_2O_3 and SiO_2 is intentionally added into the slag to meet the

✉ Cheng-bin Shi
chengbin.shi@ustb.edu.cn

✉ Ding-li Zheng
dinglizheng@wust.edu.cn

1 State Key Laboratory of Advanced Metallurgy, University of Science and Technology Beijing, Beijing 100083, China

2 College of Materials Science and Engineering, Chongqing University, Chongqing 400044, China

3 The State Key Laboratory of Refractories and Metallurgy, Wuhan University of Science and Technology, Wuhan 430081, Hubei, China

requirements for aluminum, boron and silicon target concentrations in the steel [6, 7]. The addition amount of B_2O_3 and SiO_2 in the slag is dependent on numerous factors, including the steel compositions, slag chemistry, slag amount, deoxidation scheme, furnace capacity, duration time of ESR refining, remelting rates, etc. The slag with different compositions possesses various physicochemical properties, which consequently determine largely the quality of remelted steel, such as loss and pickup of some elements in steel, inclusions, cleanliness, liquid steel solidification, surface quality of as-cast ingot, and power consumption. Therefore, studies on the slag physicochemical properties are quite important for optimizing and/ or designing the slag for ESR of a specific steel.

Crystallization properties of slag have significant effect on the initial solidification of liquid metal in mold during ESR and the surface quality of as-cast ingot [10, 13]. Many studies have been conducted to ascertain the crystallization behavior of lime–silica-based and lime–alumina-based mold fluxes for continuous casting of steel [14–17]. In view of the big difference between ESR-type slags and mold fluxes in their chemistry, great attention should be paid to reveal the crystallization characteristics of ESR-type slag. However, limited studies have been conducted in this aspect. Shi et al. [12] reported that the crystallization of ESR-type CaF_2–CaO–Al_2O_3 slag was strongly retarded by increasing SiO_2 content from 0 to 6.8 mass%. Zheng et al. [13] reported that increasing TiO_2 content of ESR-type CaF_2–CaO–Al_2O_3–MgO slag decreased the crystallization temperature and suppressed the crystallization tendency of the slag. It is highly needed to ascertain the crystallization behaviors of CaF_2–CaO–Al_2O_3 slags with varying SiO_2 and B_2O_3 addition for ESR of rotor steel.

In the current study, a series of slags were designed for ESR of rotor steel for ultra-supercritical steam turbines. The crystallization behavior of CaF_2–CaO–Al_2O_3 slags with varying SiO_2 and B_2O_3 contents was studied by differential scanning calorimetry (DSC) measurements. Continuous cooling transformation (CCT) diagrams of crystalline phases were plotted based on the DSC curves. The compositions and morphology of the crystalline phases were identified by X-ray diffraction (XRD) and scanning electron microscopy (SEM) equipped with energy dispersive spectroscopy (EDS). In addition, Raman spectroscopy was employed to analyze the slag structure and its correlation to crystallization.

2 Experimental

2.1 Sample preparation

Reagent-grade powders of CaF_2 (≥ 99.0 mass%), $CaCO_3$ (≥ 99.0 mass%), Al_2O_3 (≥ 99.99 mass%), MgO (≥ 98.5 mass%), SiO_2 (≥ 99.99 mass%) and H_3BO_3 (≥ 99.5 mass%) were used to prepare slag samples. CaO powders were produced by calcining $CaCO_3$ for 10 h in a muffle furnace at 1323 K. The thoroughly mixed powders were melted at 1773 K for 5 min in a platinum crucible to ensure complete melting and homogenization, and subsequently the liquid samples were quenched on a water-cooled copper plate. The quenched slag was then crushed and ground. All pre-melted slag samples were confirmed to be amorphous according to XRD identification, as shown in Fig. 1. The pre-melted slag samples were subjected to chemical analysis. The contents of fluorine in the slag samples were determined by ion-selective electrode method. The contents of aluminum, calcium, magnesium and boron were analyzed by inductively coupled plasma-atomic emission spectroscopy. The chemical compositions of the slag after pre-melting are listed in Table 1.

2.2 DSC measurement

Non-isothermal crystallization characteristics of the slag melts were studied using differential scanning calorimetry (Netzsch STA449F3, Netzsch Instrument Inc., Germany). About 50 mg of the slag samples were placed in a platinum crucible with an inner diameter of 5 mm and a height of 5.5 mm. The slag was heated from room temperature to 1773 K at 30 K/min and held for 1 min to eliminate bubbles and homogenize the chemical composition. It was then cooled to 623 K at various cooling rates (15, 20, and 25 K/ min). DSC measurements were taken under Ar gas atmosphere at 60 mL/min to evaluate the non-isothermal crystallization behavior of the studied slag. DSC measurement data were automatically recorded during heating and cooling cycles.
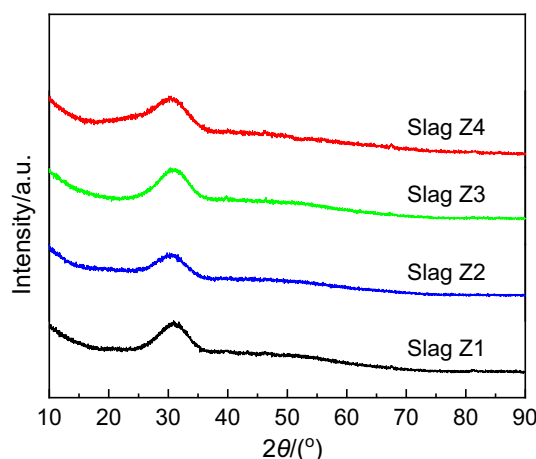

Fig. 1 XRD patterns of as-quenched slag samples. 2θ Diffraction angle

Table 1 Chemical compositions of studied slag after pre-melting (mass%)

Slag No.	CaF_2	CaO	Al_2O_3	MgO	SiO_2	B_2O_3
Z1	34.15	30.94	26.62	1.61	0.24	3.48
Z2	37.43	28.65	25.05	1.97	4.87	0
Z3	36.45	26.41	24.72	1.63	5.50	3.20
Z4	33.02	27.42	22.42	2.00	8.95	3.18

2.3 SEM–EDS and XRD analysis

After DSC measurements, solidified slag samples were mounted with epoxy resin and then polished, and then sprayed with gold and pasted with conductive adhesive to improve the electrical conductivity of the sample. SEM (FEI Quanta-250, FEI Corporation, Hillsboro, OR, USA) equipped with EDS (XFlash 5030, Bruker, Germany) was employed to determine the crystalline phases in the solidified slag.

A series of continuous cooling and quenching experiments were carried out to prepare slag samples for XRD analysis aiming to determine the crystalline phases corresponding to each exothermic peak on the DSC curves. About 2 g of slag powders were melted in a platinum crucible at 1773 K for 5 min, and then the slag powders were continuously cooled at a cooling rate of 10 K/min to the desired target temperature 10 K above the crystallization starting temperature corresponding to the exothermic peak on DSC curve with the cooling rate of 15 K/min. The slag sample was held for 20 min at the desired target temperature, and then the molten slag was quenched. The crystalline phases in the quenched slag were analyzed by XRD.

2.4 Raman spectra measurement

The quenched samples were analyzed using a Raman spectrometer (LabRAM HR Evolution, HORIBA, France). The Raman spectra were collected at room temperature in the frequency range of 200 to 2000 cm^{-1}. Raman spectra were fitted by Gauss curves.

3 Results and discussion

3.1 Crystalline phase formation and crystallization temperature

The crystallization characteristics of CaF_2–CaO–Al_2O_3–MgO–SiO_2–B_2O_3 slag with various SiO_2 and B_2O_3 contents were determined by DSC measurements at various

cooling rates. Figure 2 shows DSC curves of slag samples at cooling rates of 15, 20 and 25 K/min. It can be seen from Fig. 2 that there are three exothermic peaks on each DSC curve, which is an indication of three successive crystallization events occurring during the solidification of slag melts. According to the sequence of exothermic peaks in the cooling process, the peaks on DSC curves were designated as P1, P2 and P3, respectively.

In the continuous cooling of slag melts, the starting temperature of the exothermic peak on the DSC curves corresponds to the crystallization temperature of the crystalline phase, and the end temperature corresponds to the crystallization completion temperature. In order to reveal the crystallization behavior of the slag melts, CCT curves of crystalline phase precipitation at various cooling rates (15, 20 and 25 K/min) were established based on the sequence of exothermic peaks on the DSC curves and the corresponding starting point temperature of the crystalline phase, as shown in Fig. 3. Phase 1, Phase 2 and Phase 3 correspond to peaks P1, P2 and P3 on DSC curves in Fig. 2, respectively. It can be seen from Fig. 3 that the crystallization temperature of the crystalline phases in the slag decreases with increasing the cooling rate. A driving force is needed for crystal nucleation, and a higher cooling rate requires a greater driving force to promote crystals nucleation [12, 13]. Therefore, the crystallization temperature of the slag melts decreases with the increase in the cooling rate.

The precipitation temperature of the first crystalline phase in the continuous cooling process is defined as the crystallization temperature of the slag melts [14]. Figure 4 shows the CCT curves of the precipitation of the first crystalline phase in the slag melts with various SiO_2 and B_2O_3 contents. It can be seen from Fig. 4 that the crystallization temperature of slag melts decreases with increasing SiO_2 content from 0.24 to 8.95 mass%, indicating that the crystallization was inhibited by increasing the SiO_2 content of the slag melts. A similar trend was observed for the case where the B_2O_3 content of the slag was increased from 0 to 3.20 mass%, as shown in Fig. 4. This result is consistent with the finding reported by Wei et al. [18] for CaO–SiO_2-based slag. In the studied slag, SiO_2 and B_2O_3 addition will improve the initial solidification of liquid steel in mold and the surface quality of remelted ingot.

3.2 XRD identification of crystalline phases

In order to identify the types of crystalline phases corresponding to the exothermic peaks on the DSC curves, the crystalline phases at different temperatures were determined by XRD measurements. A series of continuous cooling measurements at cooling rate of 10 K/min were
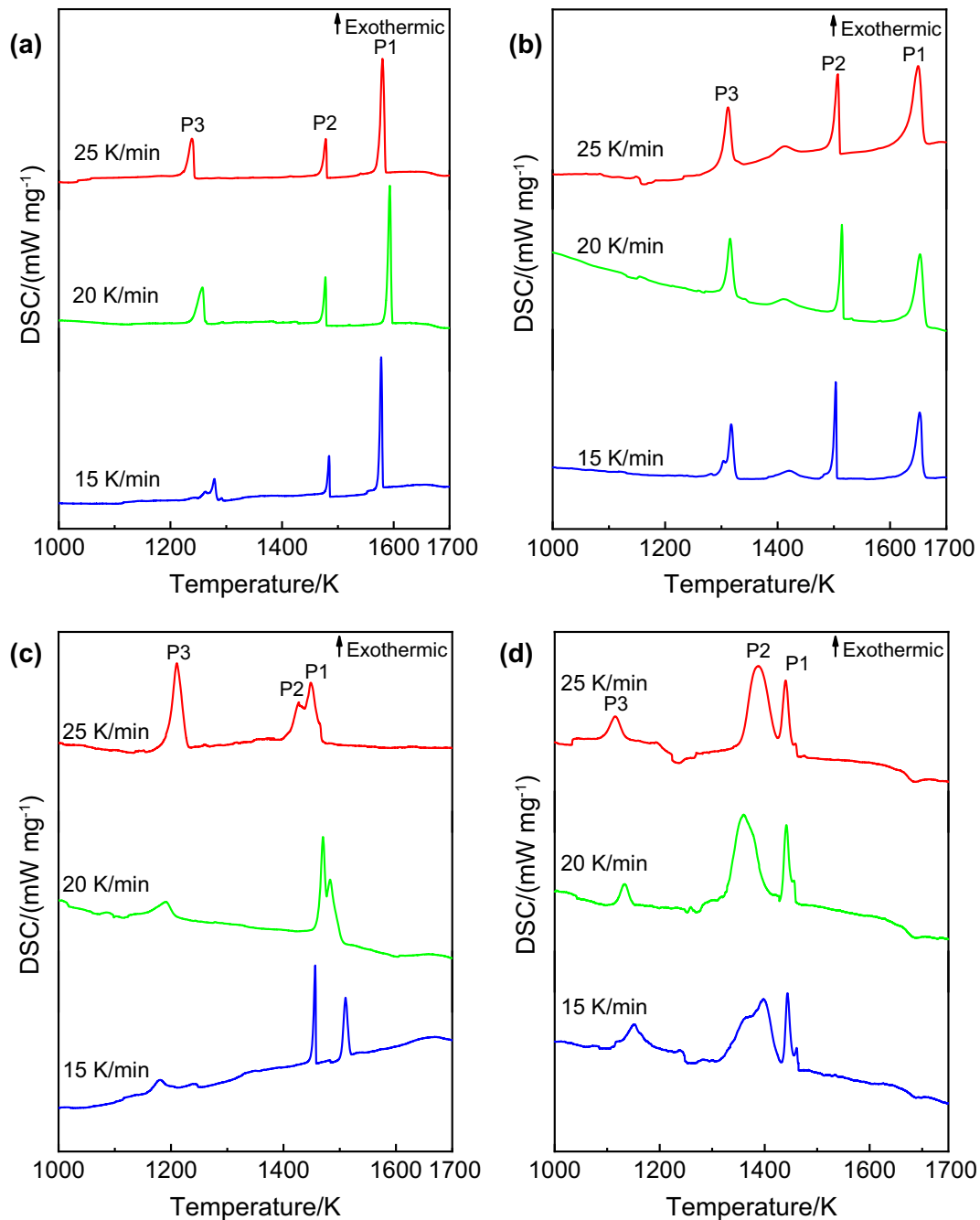
Fig. 2 DSC curves of non-isothermal crystallization of slag melts at various cooling rates. **a** Slag Z1; **b** Slag Z2; **c** Slag Z3; **d** Slag Z4

carried out to prepare slag samples for XRD identification because the slag amount after DSC measurements is too small. In order to ensure that only first crystalline phase precipitates during the continuous cooling process, the temperature was continuously cooled to the desired target temperature (10 K above the crystallization starting temperature corresponding to the first exothermic peak (P1) on DSC curve) with the cooling rate of 15 K/min. Similarly, in order to ensure only the first and second crystalline phases precipitate and prevent the precipitation of the third

crystalline phase, the temperature was continuously cooled to the temperature which was 10 K higher than that of the second temperature crystallization phase. The precipitation of all crystalline phases in continuous cooling of slag melts has completed at 773 K.

According to the measured starting temperatures of exothermic peaks on the DSC curves shown in Fig. 2, the types of crystalline phases and their precipitation order in slag melts were determined by XRD. The XRD results of quenched slag samples at different temperatures are shown
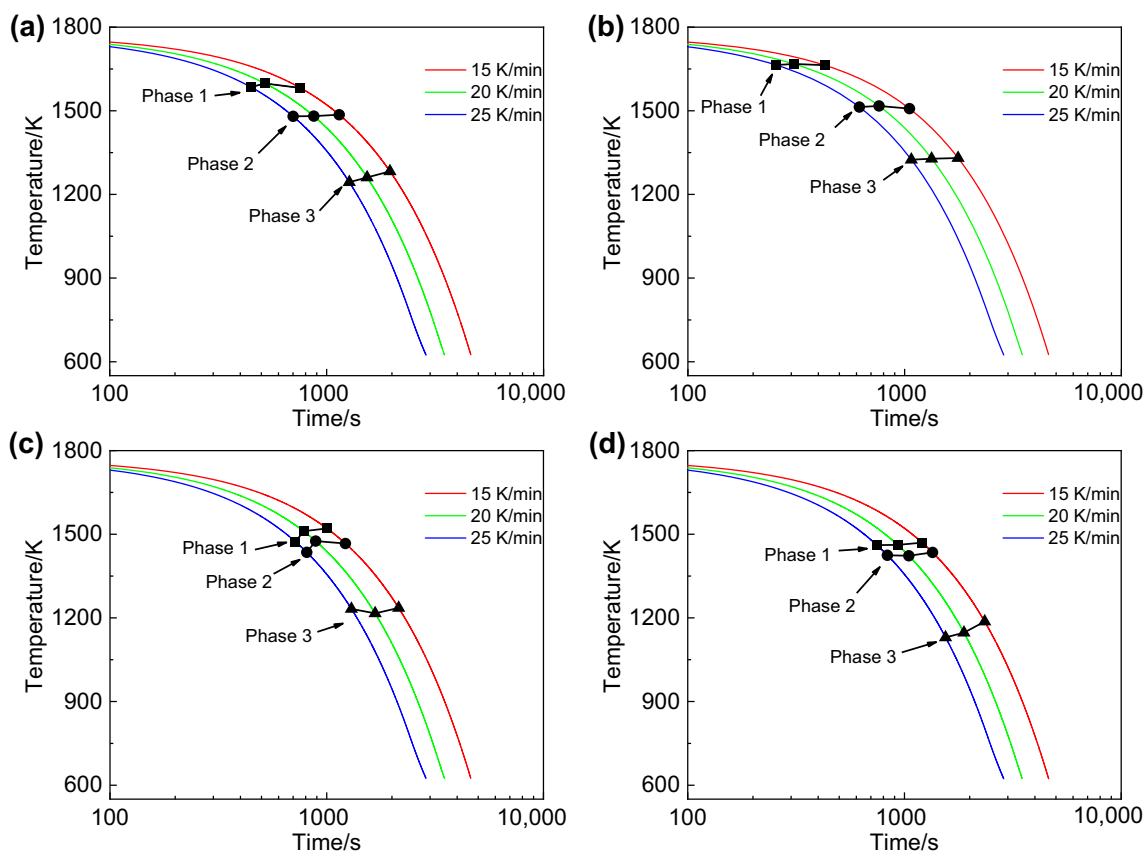
Fig. 3 CCT diagrams of slag melts with different SiO_2 and B_2O_3 contents. **a** Slag Z1; **b** Slag Z2; **c** Slag Z3; **d** Slag Z4
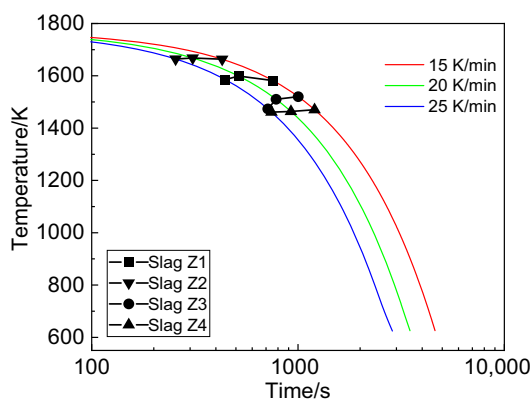

Fig. 4 CCT diagram for first crystalline phase precipitated in slag

in Fig. 5. Only crystalline phase $11CaO\cdot7Al_2O_3\cdot CaF_2$ is detected by XRD analysis at the higher temperature as shown in Fig. 5. Crystalline phases $11CaO\cdot7Al_2O_3\cdot CaF_2$ and CaF_2 are detected by XRD at medium temperature. At the lowest temperature of 773 K, three crystalline phases are presented, i.e., $11CaO\cdot7Al_2O_3\cdot CaF_2$, CaF_2 and $MgO\cdot Al_2O_3$ (or MgO). Comparing these crystalline phases at three different temperatures, it can be concluded that the first crystalline phase precipitated in the continuous cooling of slag melts is $11CaO\cdot7Al_2O_3\cdot CaF_2$, followed by

crystalline phase CaF_2 and the third crystalline phase $MgO\cdot Al_2O_3$ (or MgO). In the current study, the types of the first and second crystalline phase precipitated during slag melts cooling are consistent with $CaO–Al_2O_3–CaF_2$ phase diagram [19]. Increasing SiO_2 content from 0.24 to 8.95 mass% and B_2O_3 from 0 to 3.20 mass% in the slag did not change the types of crystalline phases and their precipitation sequence.

3.3 SEM–EDS observation of crystalline phases in slag

The morphology and compositions of crystalline phases in slag after DSC measurements were identified by SEM–EDS. The different cooling rates herein have no influence on the precipitation sequence of the crystalline phases. Therefore, the morphology, size and compositions of crystalline phases of the slag samples after DSC measurements at a cooling rate of 20 K/min were analyzed by SEM–EDS. Combined with DSC and XRD results, the types of crystalline phases, the precipitation sequence and the corresponding XRD and EDS results are summarized and shown in Table 2. Figure 6 shows the SEM–EDS results of the solidified slag.
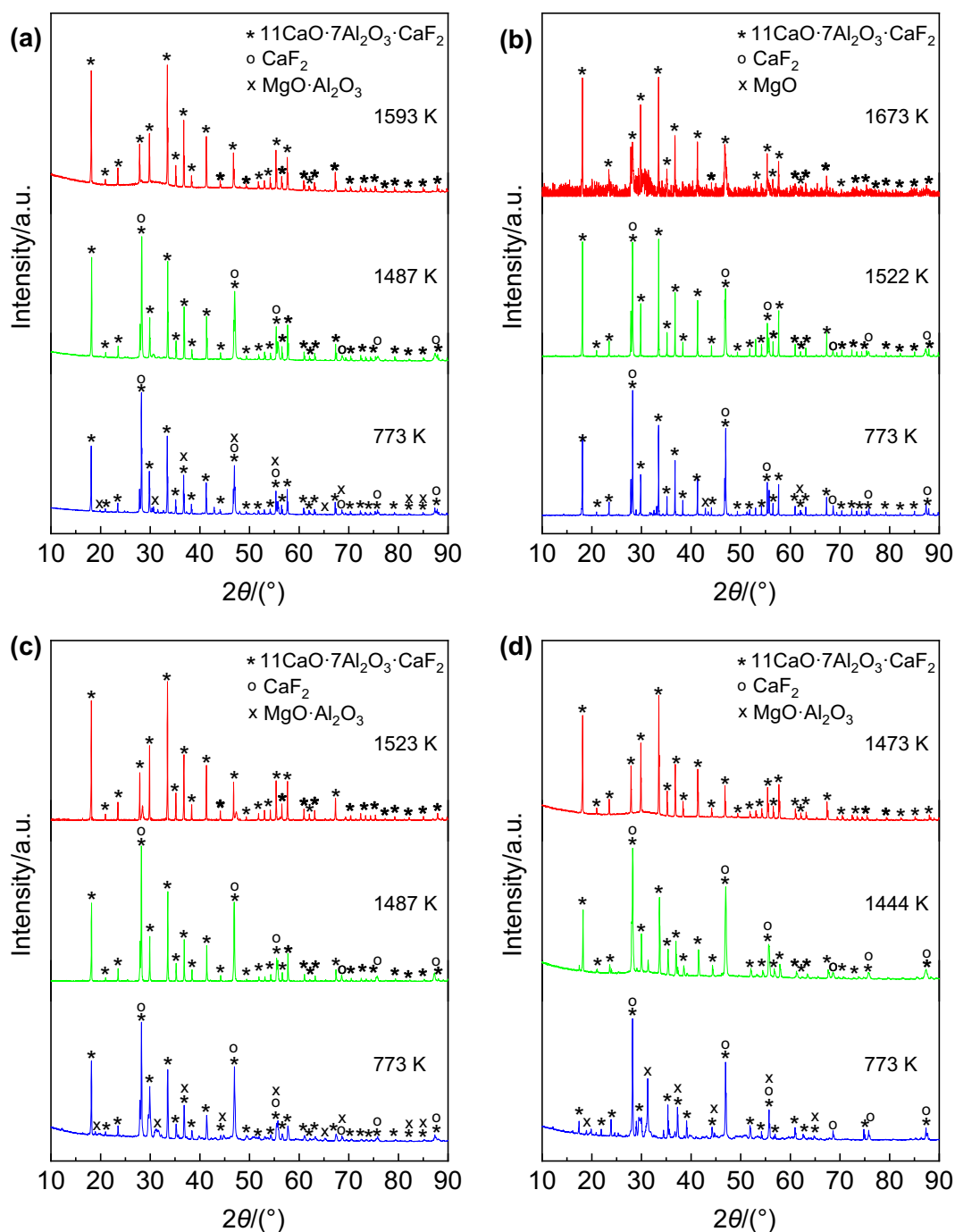
Fig. 5 XRD patterns of slag quenched at desired temperatures. **a** Slag Z1; **b** Slag Z2; **c** Slag Z3; **d** Slag Z4

It can be seen from Fig. 6 that three crystalline phases are presented in each slag. The results in Table 2 show that three crystalline phases, $11CaO \cdot 7Al_2O_3 \cdot CaF_2$, CaF_2 and $MgO \cdot Al_2O_3$ (or MgO), are consistent with the results of XRD shown in Fig. 5. According to SEM–EDS results, the main crystalline phase in the solidified slag is faceted $11CaO \cdot 7Al_2O_3 \cdot CaF_2$, which occupies the largest area fraction, and the crystals are bonded together. CaF_2 crystals

are faceted or spherical and distribute among $11CaO \cdot 7Al_2O_3 \cdot CaF_2$ crystals. Non-faceted $MgO \cdot Al_2O_3$ (or MgO) crystals unevenly distribute in the slag. It is noted that the sizes of crystalline phases $11CaO \cdot 7Al_2O_3 \cdot CaF_2$ and CaF_2 decrease with the increase in SiO₂ (0.24–8.95 mass%) and B₂O₃ (0–3.20 mass%) contents. It originates from the decrease in the crystallization of the molten slag with increasing SiO₂ and B₂O₃ contents, which is

Table 2 XRD analysis results and compositions of crystals determined by EDS in slag after DSC measurements

Slag No.	Exothermic peak on DSC curves	Crystalline phase identified by XRD	Element/at.%				
			O	Ca	Al	F	Mg
Z1	P1	$11CaO \cdot 7Al_2O_3 \cdot CaF_2$	42.11	30.44	23.32	4.13	–
	P2	CaF_2	–	36.40	–	63.60	–
	P3	$MgO \cdot Al_2O_3$	45.96	–	32.83	–	21.21
Z2	P1	$11CaO \cdot 7Al_2O_3 \cdot CaF_2$	46.28	28.96	20.17	4.59	–
	P2	CaF_2	–	36.99	–	63.01	–
	P3	MgO	41.59	–	–	–	58.41
Z3	P1	$11CaO \cdot 7Al_2O_3 \cdot CaF_2$	41.47	31.15	22.77	4.91	–
	P2	CaF_2	–	38.46	–	61.54	–
	P3	$MgO \cdot Al_2O_3$	48.41	–	33.18	–	18.41
Z4	P1	$11CaO \cdot 7Al_2O_3 \cdot CaF_2$	44.78	29.55	21.92	3.75	–
	P2	CaF_2	–	41.24	–	58.76	–
	P3	$MgO \cdot Al_2O_3$	49.92	–	32.00	–	18.08
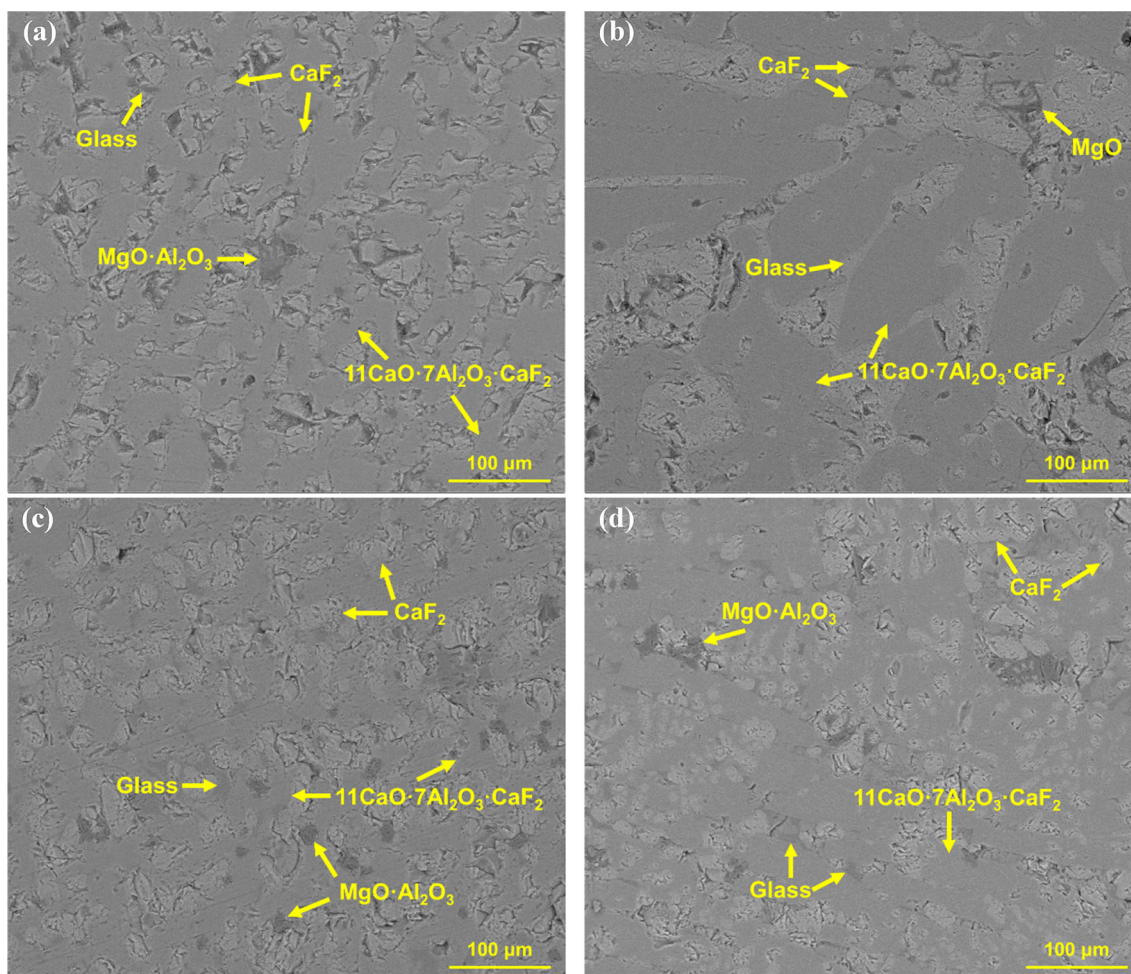
Fig. 6 SEM images of solidified slag after DSC measurements at cooling rate of 20 K/min. **a** Slag Z1; **b** Slag Z2; **c** Slag Z3; **d** Slag Z4

unfavorable to the nucleation and growth of crystals in slag melts, as discussed in Sect. 3.1. Crystallization consists of both nucleation and crystal growth processes, which is closely related to the slag structure. The influence of SiO_2 and B_2O_3 on slag structure and its correlation with crystallization will be discussed in Sect. 3.4.

3.4 Role of SiO₂ and B₂O₃ on slag structure and its correlation with crystallization

Crystallization behavior of slag melts is closely related to the structure characteristics. Raman spectroscopy can provide semi-quantitative information of slag structure, which can be used to characterize the structure evolution of the slag with varying SiO_2 and B_2O_3 contents. Figure 7 presents the original Raman spectra of CaF_2–CaO–Al_2O_3–MgO–SiO_2–B_2O_3 slag with various SiO_2 and B_2O_3 contents.

It can be seen from Fig. 7 that there are three obvious peaks located in the low-frequency region at around 550 cm^{-1}, the medium-frequency region of 680–890 cm^{-1}, and the high-frequency region near 920 cm^{-1}, respectively. It can be seen from Fig. 7a that the relative height of the peak in the medium-frequency region significantly increases with the increase in the SiO_2 content of the slag, indicating an increase in the relative fraction of structure units in the medium-frequency region. The relative height of the peak in the high-frequency region is observed to significantly increase with increasing the B_2O_3 contents of the slag as shown in Fig. 7b, indicating an increase in the relative fraction of structure units in the high-frequency region. In order to further analyze the changes of the structure units relative fraction of each functional group in the slag with various SiO_2 and B_2O_3 contents, the Raman curves were deconvolved by Gaussian fitting similar to the method used by Mysen et al. [20]. The

Raman shifts range from 500 to 1000 cm^{-1}, and the correlation coefficient r^2 is no less than 0.99. The results of deconvoluted Raman spectra are shown in Fig. 8. The assignments of Raman shift for different structure units are summarized in Table 3.

The deconvolution results of Raman spectra of quenched slags with different SiO_2 and B_2O_3 contents are shown in Fig. 8. At the low-frequency region of 550 cm^{-1}, two spectral peaks were resolved. The Raman shift at around 550 cm^{-1} is assigned to transverse motion of bridged oxygen within Al–O–Al linkages [21–23]. The bands centered near 600 cm^{-1} is related to $[AlO_6]$ stretching vibration [24–26]. The Raman shifts at 720, 740, 760, 780 and 830 cm^{-1} are assigned to $[AlO_4]$ stretching vibration Q_{Al}^i ($i = 0$, 1, 2, 3 and 4) structure units [21, 27–29]. The Raman shift around at 865 cm^{-1} is assigned to Si–O–Al structure units [30, 31]. The Raman shift at about 920 cm^{-1} is attributed to the symmetric stretching vibrations of $[BO_4]$ structure units [32, 33]. As can be seen from Fig. 8a, c and d, with the increase in SiO_2 content in the slag, the intensity of spectral peak corresponding to Si–O–Al structure units is significantly enhanced. This is because Si–O⁻ vibration increases with the increase in SiO_2 content, which is conducive to the $[AlO_4]$ structure participating in the silicate network structure to form complex Si–O–Al structure units, resulting in the increase in the amount of slag network formers and the degree of molten slag polymerization. The deconvolution results of Raman spectra of slag samples with varying B_2O_3 contents are shown in Fig. 8b and c, with the increase in the B_2O_3 content, the relative height of the spectral peaks around 920 cm^{-1} in the high-frequency region increased significantly. It indicated that new structure units $[BO_4]$ were formed with the addition of B_2O_3 into the slag.
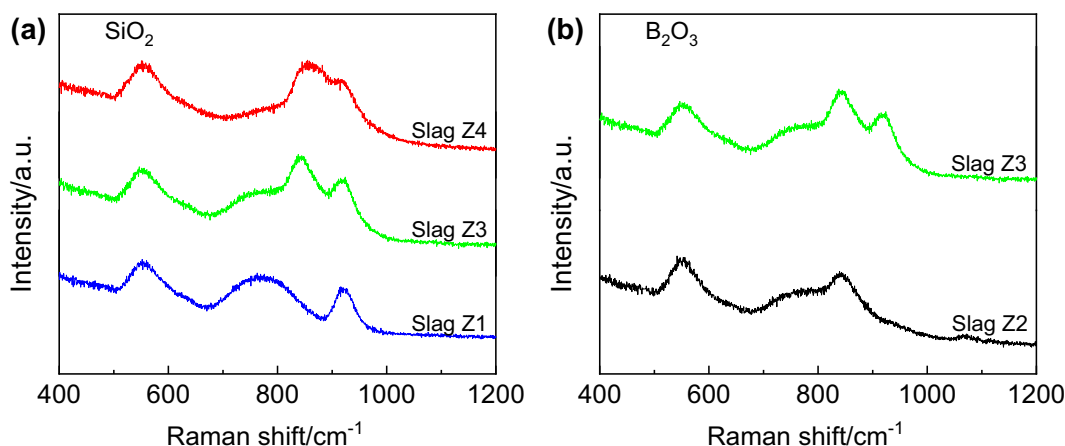

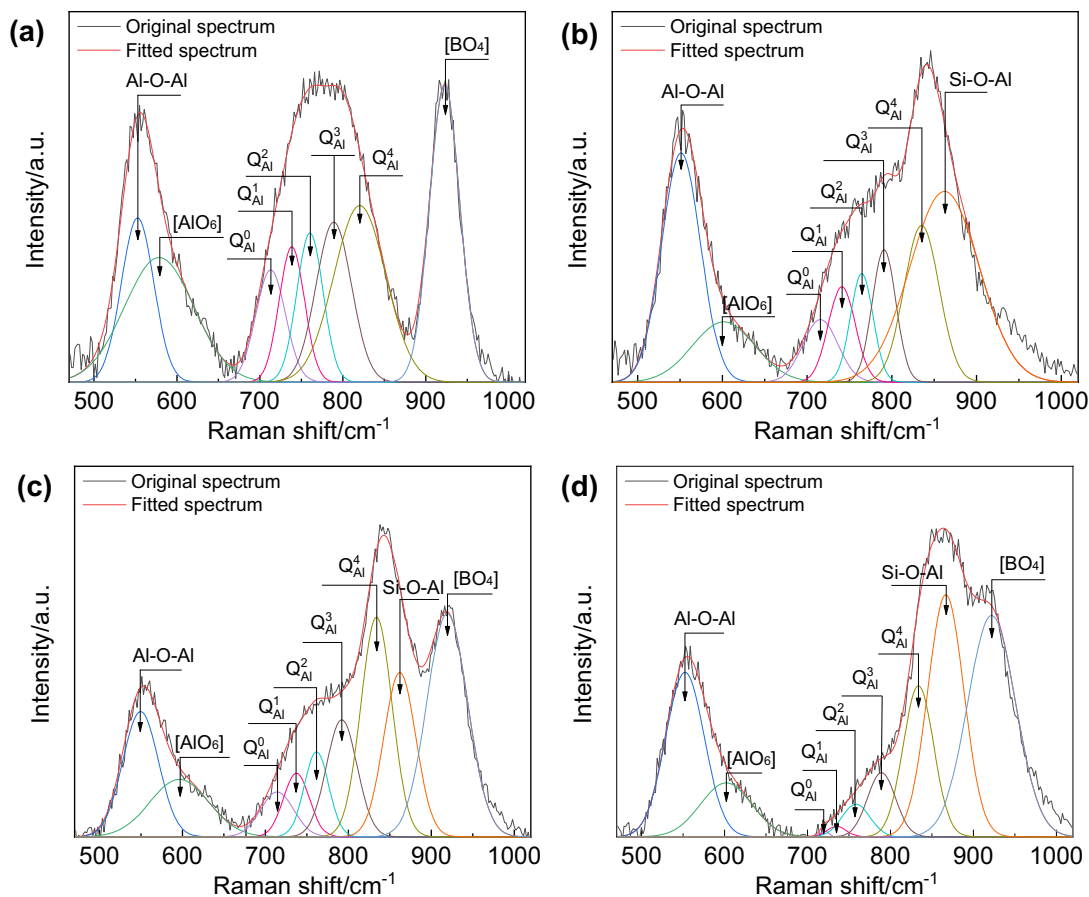**Fig. 7** Original Raman spectra of slag with varying SiO_2 and B_2O_3 contents

Fig. 8 Deconvoluted Raman spectra of quenched slag with varying SiO_2 and B_2O_3 contents. **a** Slag Z1; **b** Slag Z2; **c** Slag Z3; **d** Slag Z4

Table 3 Assignments of Raman bands in spectra of CaF_2–CaO–Al_2O_3–MgO–SiO_2–B_2O_3 slag

Raman shift/cm^{-1}	Raman assignment	Refs.
549–552	Al–O–Al linkages	[21–23]
578–609	$[AlO_6]$ units	[24–26]
712–720	Q_{Al}^0 units	[21, 27–29]
735–738	Q_{Al}^1 units	[21, 27–29]
758–765	Q_{Al}^2 units	[21, 27–29]
788–795	Q_{Al}^3 units	[21, 27–29]
820–836	Q_{Al}^4 units	[21, 27–29]
859–870	Si–O–Al units	[30, 31]
918–922	$[BO_4]$ units	[32, 33]

Figure 9 shows the variation of relative fraction of structure units in CaF_2–CaO–Al_2O_3–MgO–SiO_2–B_2O_3 slag with various SiO_2 (0.24–8.95 mass%) and B_2O_3 (0–3.20 mass%) contents. It can be seen from Fig. 9a that, with the increase in SiO_2 content in the slag, the relative fractions of Q_{Al}^i ($i = 0, 1, 2, 3,$ and 4) and $[AlO_6]$ octahedron structure units decrease, and the relative fractions of Al–O–Al, Si–

O–Al and $[BO_4]$ structure units increase. As can be seen from Fig. 9b, with the increase in B_2O_3 content of the slag, the relative fractions of Q_{Al}^i ($i = 0, 1,$ and 2), Al–O–Al and Si–O–Al structure units decrease, and the relative fractions of Q_{Al}^i ($i = 3$ and 4) and $[BO_4]$ structure units increase. The relative fraction of the $[AlO_6]$ structure units exhibits no influence with increasing the B_2O_3 content of the slag. Due to the charge compensation of Al^{3+} ions in the studied slag, free O^{2-} ions and metal cation (Ca^{2+}) were consumed to form $[AlO_4]$ tetrahedron structure units. In order to reveal the change of the polymerization degree of $[AlO_4]$ tetrahedron structure, the number of non-bridged oxygen in $[AlO_4]$ tetrahedron structure can be calculated by multiplying the non-bridging oxygen number of Q_{Al}^i ($i = 0, 1, 2, 3,$ and 4) structure units by its area ratio in the Raman spectra [21, 27, 28]. It could be observed from Table 4 that the number of non-bridging oxygen (NBO/T) in $[AlO_4]$ tetrahedron structure decreases from 0.766 to 0.123 and 0.589 to 0.493 with the increase in SiO_2 (0.24–8.95 mass%) and B_2O_3 (0–3.20 mass%) contents, indicating that the polymerization degree of $[AlO_4]$ tetrahedron structure is increased.
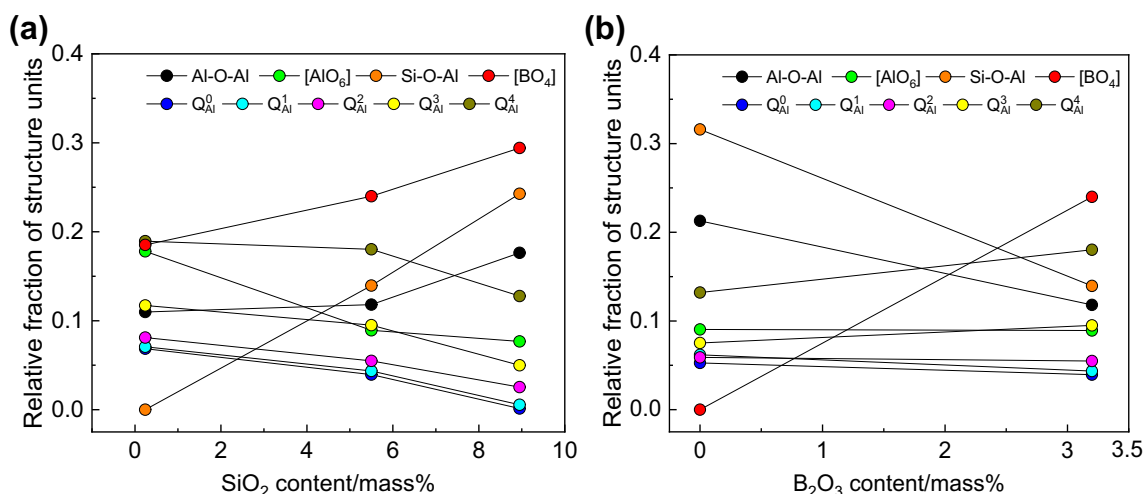
Fig. 9 Relative fraction of structure units in CaF₂–CaO–Al₂O₃–MgO–SiO₂–B₂O₃ slag with various SiO₂ and B₂O₃ contents

Table 4 Relative fraction of structure units and non-bridged oxygen number of structure units Q_{Al}^i (i = 0, 1, 2, 3, and 4)

Slag No.	Relative fraction of structure units					NBO/T
	Q_{Al}^0	Q_{Al}^1	Q_{Al}^2	Q_{Al}^3	Q_{Al}^4	
Z1	0.069	0.071	0.081	0.117	0.189	0.766
Z2	0.053	0.062	0.059	0.075	0.132	0.589
Z3	0.039	0.044	0.055	0.095	0.180	0.493
Z4	0.001	0.006	0.025	0.050	0.128	0.123

In the studied slag, basic metal oxides are consumed to form [AlO₄] and [BO₄] structure units because of the charge compensation effect of Al^{3+} and B^{4+} ions. As shown in Fig. 9a, the relative fraction of [BO₄] structure units increases with the increase in SiO₂ content in the slag. It could be inferred that more basic metal oxides participated in the charge compensation of B^{3+} ions to form [BO₄] structure units with the addition of SiO₂ in the slag. The relative fraction of [AlO₆] structure units decreases with the increase in SiO₂ content of the slag, indicating that more Al^{3+} ions are transformed to [AlO₄] by charge compensation. The relative fraction of Si–O–Al structure units increases with increasing the SiO₂ content of slag, originating from the combination of [SiO₄] and [AlO₄] tetrahedral structure units to form Si–O–Al structure units [34–36].

B₂O₃ usually acts as an acidic oxide that forms a network structure in the slag with the modifier content (CaO in the current slag) less than 30 mass% [34, 37, 38]. Therefore, it is deduced that B₂O₃ exists in the form of [BO₄] structure units in the studied slag. The basic metal oxides (CaO) gave priority to compensating the [BO₄] structure units, resulting that the relative fractions of Al–O–Al and

Si–O–Al structure units decrease with the addition of B₂O₃ in the slag. Furthermore, Q_{Al}^i (i = 0, 1, and 2) structure units were compensated into more complex Q_{Al}^i (i = 3 and 4) structure units because of the consumption of free O^{2-} ions and metal cations (Ca^{2+}) in the slag. Thus, the number of bridging oxygen in [AlO₄] tetrahedron structure units increases, indicating that the polymerization degree of [AlO₄] tetrahedron structural increases. Increasing B₂O₃ content of the slag has no influence on the relative fraction of [AlO₆] octahedron structure units as shown in Fig. 9b. Therefore, the polymerization degree of slag increases with the addition of B₂O₃, which results from that part of bridging oxygens in Al–O–Al and Si–O–Al are transferred to form complex [BO₄] structure units, and simpler structure units of Q_{Al}^i (i = 0, 1, and 2) formed more complex Q_{Al}^i (i = 3 and 4) structure units because of the consumption of free O^{2-} ions and metal cations (Ca^{2+}) in the slag.

The nucleation and growth of crystals are related to slag structure. With the increase in SiO₂ and B₂O₃ contents of the slag, more metal cations (Ca^{2+}) were consumed for charge compensation of Al^{3+} ions. [AlO₄] in the slag combines with [SiO₄] to form Al–O–Al and Si–O–Al structure units, thus increasing the amount of network formers and the polymerization degree of the slag. In this case, the diffusion of slag components in the slag is retarded, which is unfavorable to the precipitation of crystalline phases, leading to weakening of the slag melts crystallization.

4 Conclusions

1. The crystallization temperature of the slag melts decreases with increasing the SiO₂ content from 0.24 to 8.95 mass% in the slag, and the crystallization

tendency of the slag is inhibited. Increasing B_2O_3 content from 0 to 3.20 mass% exhibits a same effect.

2. In the cooling of CaF_2–CaO–Al_2O_3–MgO–SiO_2–B_2O_3 slag melts, $11CaO \cdot 7Al_2O_3 \cdot CaF_2$, CaF_2 and $MgO \cdot Al_2O_3$ (or MgO) crystalline phases precipitate in sequence irrespective of SiO_2 and B_2O_3 contents of the slag. The main crystalline phase in the slag is $11CaO \cdot 7Al_2O_3 \cdot CaF_2$. The sizes of $11CaO \cdot 7Al_2O_3 \cdot CaF_2$ and CaF_2 crystals decrease with the increase in the SiO_2 and B_2O_3 contents due to suppression of slag crystallization.

3. The polymerization degree of CaF_2–CaO–Al_2O_3-based slag melts increases with increasing the SiO_2 content of the slag. It is because more basic metal oxides (CaO) are consumed for charge compensation of Al^{3+} and B^{3+} ions with increasing the SiO_2 content, resulting in a decrease in the modifier amount of the slag melts. On the other hand, it is due to the fact that more $[SiO_4]$ tetrahedral structure units connect with $[AlO_4]$ tetrahedral structure units to form complex Si–O–Al structure units in the slag melts.

4. With the addition of B_2O_3 in the slag, a part of the bridging oxygens in Al–O–Al and Si–O–Al were transferred to form complex $[BO_4]$ structure units, and simpler structure units of Q_{Al}^i ($i = 0$, 1 and 2) were compensated in more complex Q_{Al}^i ($i = 3$ and 4) structure units because of the consumption of free O^{2-} ions and metal cations (Ca^{2+}) in the slag. The degree of polymerization of the slag increases with increasing SiO_2 and B_2O_3 contents, which results in inhibition of slag melts crystallization.

References

[1] F. Abe, M. Tabuchi, H. Semba, M. Igarashi, M. Yoshizawa, N. Komai, A. Fujita, in: Proceedings of the 5th International Conference on Advances in Materials Technology for Fossil Power Plants, Marco Island, Florida, USA, 2007, pp. 92–106.

[2] P. Yan, Z.D. Liu, H.S. Bao, Y.Q. Weng, W. Liu, Mater. Sci. Eng. A 588 (2013) 22–28.

[3] K.C. Kim, Y.W. Ma, B.O. Kong, M.S. Kim, S.T. Kang, Mater. Res. Innovat. 17 (2013) 332–336.

[4] A. Azeez, R. Eriksson, D. Leidermark, M. Calmunger, Theoret. Appl. Fract. Mech. 107 (2020) 102510.

[5] X. Xu, A. Benaarbia, D.J. Allen, M.A.E. Jepson, W. Sun, Mater. Sci. Eng. A 791 (2020) 139546.

[6] D.S. Kim, G.J. Lee, M.B. Lee, J.I. Hur, J.W. Lee, in: Proc. 2015 Int. Symp. on Liquid Metal Processing and Casting, The Minerals, Metals and Materials Society, Warrendale, PA, USA, 2015, pp. 43–52.

[7] J.T. Ba, J.J. Gao, S.B. Wang, Q.M. Yang, Heavy Casting and Forging (2018) No. 3, 1–4.

[8] Y.L. Luo, L.L. Li, Y.J. He, Heavy Casting and Forging (2016) No. 2, 3–5.

[9] D.L. Zheng, J. Li, C.B. Shi, J. Zhang, R.M. Geng, ISIJ Int. 60 (2020) 1577–1585.

[10] C.B. Shi, D.L. Zheng, S.H. Shin, J. Li, J.W. Cho, Int. J. Miner. Metall. Mater. 24 (2017) 18–24.

[11] X.J. Wang, Y. Liu, G.Q. Li, Q. Wang, T.F. Li, Y.X. Cao, Vacuum 185 (2021) 109997.

[12] C.B. Shi, J. Li, J.W. Cho, F. Jiang, I.H. Jung, Metall. Mater. Trans. B 46 (2015) 2110–2120.

[13] D.L. Zheng, J. Li, C.B. Shi, J.T. Ju, Metall. Mater. Trans. B 50 (2019) 1148–1160.

[14] C.B. Shi, M.D. Seo, J.W. Cho, S.H. Kim, Metall. Mater. Trans. B 45 (2014) 1081–1097.

[15] B.X. Lu, W.L. Wang, Metall. Mater. Trans. B 46 (2015) 852–862.

[16] J.W. Cho, K. Blazek, M. Frazee, H.B. Yin, J.H. Park, S.W. Moon, ISIJ Int. 53 (2013) 62–70.

[17] T. Wu, Q. Wang, S. He, J. Xu, X. Long, Y. Lu, Steel Res. Int. 83 (2012) 1194–1202.

[18] J. Wei, W.L. Wang, L.J. Zhou, D.Y. Huang, H. Zhao, F.J. Ma, Metall. Mater. Trans. B 45 (2014) 643–652.

[19] R.H. Nafziger, High Temp. Sci. 5 (1973) 414–422.

[20] B.O. Mysen, L.W. Finger, D. Virgo, F.A. Seifert, Am. Miner. 67 (1982) 686–695.

[21] P. McMillan, B. Piriou, J. Non-Cryst. Solids 55 (1983) 221–242.

[22] M. Licheron, V. Montouillout, F. Millot, D.R. Neuville, J. Non-Cryst. Solids 357 (2011) 2796–2801.

[23] P.L. Higby, R.J. Ginther, I.D. Aggarwal, E.J. Friebele, J. Non-Cryst. Solids 126 (1990) 209–215.

[24] J.H. Park, D.J. Min, H.S. Song, ISIJ Int. 42 (2002) 38–43.

[25] P. Tarte, Spectrochim. Acta 23A (1967) 2127–2143.

[26] J. Qi, C. Liu, M. Jiang, J. Non-Cryst. Solids 475 (2017) 101–107.

[27] T.S. Kim, J.H. Park, ISIJ Int. 54 (2014) 2031–2038.

[28] L.G. Hwa, S.L. Hwang, L.C. Liu, J. Non-Cryst. Solids 238 (1998) 193–197.

[29] J.L. Li, K.C. Chou, Q.F. Shu, ISIJ Int. 60 (2020) 51-57.

[30] J.X. Gao, G.H. Wen, T. Huang, B.W. Bai, P. Tang, Q. Liu, J. Non-Cryst. Solids 452 (2016) 119–124.

[31] J.H. Park, D.J. Min, J. Non-Cryst. Solids 337 (2004) 150–156.

[32] X.Y. Fan, J.L. Zhang, K.X. Jiao, R.Z. Xu, K.D. Wang, Metall. Res. Technol. 115 (2018) 313.

[33] J. Yang, J.Q. Zhang, O. Ostrovski, C. Zhang, D.X. Cai, Metall. Mater. Trans. B 50 (2019) 291–303.

[34] X.H. Huang, J.L. Liao, K. Zheng, H.H. Hu, F.M. Wang, Z.T. Zhang, Ironmak. Steelmak. 41 (2014) 67–74.

[35] S.K. Lee, J.F. Stebbins, J. Non-Cryst. Solids 270 (2000) 260–264.

[36] Z.J. Wang, I. Sohn, J. Am. Ceram. Soc. 101 (2018) 4285–4296.

[37] K.C. Mills, C.Å. Däcker, The casting powders book, Springer, New York, USA, 2017.

[38] X.B. Yan, W.J. Pan, X.S. Wang, X.B. Zhang, S.P. He, Q. Wang, Metall. Mater. Trans. B 52 (2021) 2526–2535.